Draft version December 21, 2023
Typeset using LaTeX **twocolumn** style in AASTeX63

Stellar Flares Are Far-Ultraviolet Luminous

Vera L. Berger,[1,2,3,*] Jason T. Hinkle,[2,†] Michael A. Tucker,[4,5,‡] Benjamin J. Shappee,[2]
Jennifer L. van Saders,[2] Daniel Huber,[2,6] Jeffrey W. Reep,[7] Xudong Sun (孙旭东),[7] and Kai E. Yang (杨凯)[7]

[1] *Cavendish Laboratory, Department of Physics, University of Cambridge, JJ Thomson Avenue, Cambridge, CB3 0HE, UK*
[2] *Institute for Astronomy, University of Hawai'i, 2680 Woodlawn Drive, Honolulu, HI 96822, USA*
[3] *Department of Physics and Astronomy, Pomona College, 333 N. College Way, Claremont, CA 91711, USA*
[4] *Department of Astronomy, The Ohio State University, 140 West 18th Avenue, Columbus, OH 43210, USA*
[5] *Center for Cosmology and Astroparticle Physics, The Ohio State University, 191 W. Woodruff Avenue, Columbus, OH 43210, USA*
[6] *Sydney Institute for Astronomy (SIfA), School of Physics, University of Sydney, NSW 2006, Australia*
[7] *Institute for Astronomy, University of Hawai'i, 34 Ohia Ku St., Pukalani, HI 96768, USA*

Submitted to MNRAS

ABSTRACT

We identify 182 flares on 158 stars within 100 pc of the Sun in both the near-ultraviolet (NUV: 1750 – 2750 Å) and far-ultraviolet (FUV: 1350 – 1750 Å) using high-cadence light curves from the *Galaxy Evolution Explorer (GALEX)*. Ultraviolet (UV) emission from stellar flares plays a crucial role in determining the habitability of exoplanetary systems. However, whether such UV emission promotes or threatens such life depends strongly on the energetics of these flares. Most studies assessing the effect of flares on planetary habitability assume a 9 000 K blackbody spectral energy distribution that produces more NUV flux than FUV flux ($\mathcal{R} \equiv F_{\rm FUV}/F_{\rm NUV} \approx \frac{1}{6}$). Instead, we observe the opposite with the excess FUV reaching $\mathcal{R} \approx \frac{1}{2} - 2$, roughly $3 - 12$ times the expectation of a 9 000 K blackbody. The ratio of FUV to NUV time-integrated flare energies is 3.0 times higher on average than would be predicted by a constant 9 000 K blackbody during the flare. Finally, we find that the FUV/NUV ratio at peak tentatively correlates ($\sim 2\sigma$ significance) both with total UV flare energy and with the $G-RP$ color of the host star. On average, we observe higher FUV/NUV ratios at peak in $E_{\rm UV} > 10^{32}$ erg flares and in flares on fully convective stars.

Keywords: stars: flare – stars: low-mass – ultraviolet: stars – astrobiology

1. INTRODUCTION

Stellar flares are energetic bursts of electromagnetic radiation driven by magnetic reconnection (e.g., Litvinenko 1999; Benz & Güdel 2010; Shibata & Takasao 2016). Flares are more frequently observed on low-mass stars ($M < 1.5 M_\odot$), which have surface convection zones (e.g., Pettersen 1989; Balona et al. 2015; Davenport 2016; Doorsselaere et al. 2017). Flares on M-dwarf stars are of particular interest because of these stars' heightened magnetic activity and ideal candidacy to detect exoplanets in the habitable zone (e.g., Endl et al. 2003; Kaltenegger & Traub 2009; Reiners 2012).

Ultraviolet emission from flares impacts the habitability of exoplanets orbiting flaring stars. Rimmer et al. (2018) delineated "abiogenesis zones" in which flare rates and energies could deliver sufficient UV photons to drive prebiotic chemistry. On the other hand, Tilley et al. (2019) characterized "ozone depletion zones" in which M-dwarf flares of sufficient rates and energies deplete the ozone column of habitable exoplanets. Flares with energies above 10^{34} erg may contribute to either effect. Thus, for sufficiently high flare rates, it is unclear exactly where flares help versus hinder the development of complex molecules.

Recent optical studies have found few stars that display superflare ($E > 10^{33}$ erg) rates and energies sufficient to affect exoplanet habitability (Schmidt et al.

Corresponding author: Vera Berger
vlb36@cam.ac.uk

* Churchill Scholar
† FINESST FI
‡ CCAPP Fellow

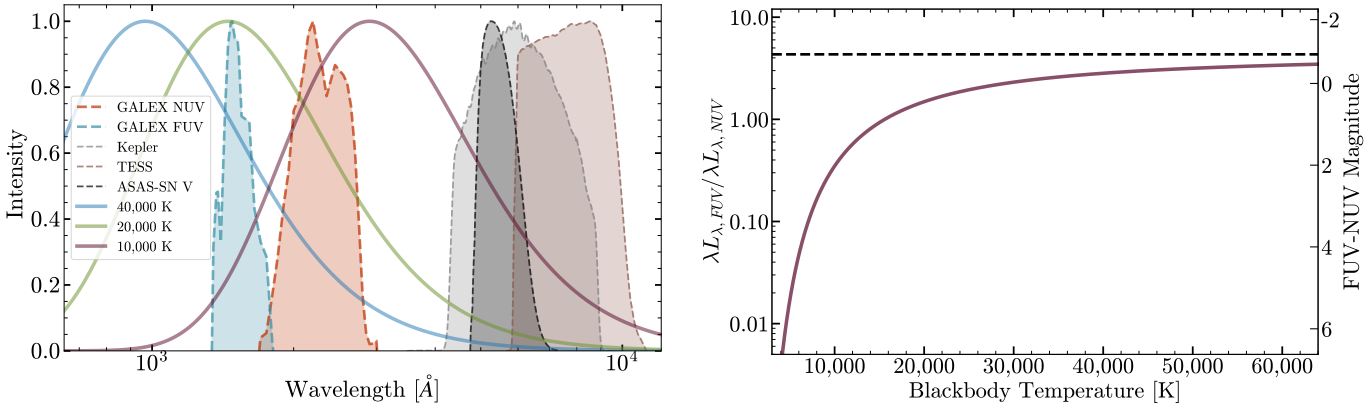

Figure 1. *Left panel:* Normalized blackbody curves (solid lines) spanning a range of observed temperatures plotted against filter response functions (dashed lines) for telescopes commonly used for flare studies. The TESS (brown), *Kepler* (black), and ASAS-SN V band (gray) response functions fall on the Rayleigh-Jeans tail for temperatures above $\sim 7\,000$ K. *GALEX* NUV (red) and FUV (teal) filter response functions fall around the peaks of blackbody SEDs for temperatures $\sim 10\,000 - 30\,000$ K. *Right panel:* Relation between blackbody temperature and FUV/NUV λL_λ ratio, computed using synthetic photometry. The dashed line at 4.33 denotes the numerically-computed asymptote once the *GALEX* filters are both in the Rayleigh-Jeans limit.

2014, 2016, 2019; Rodríguez et al. 2018; Rodríguez Martínez et al. 2020; Günther et al. 2020; Feinstein et al. 2020; Zeldes et al. 2021; Bogner et al. 2021). These studies typically assume a constant-temperature blackbody spectrum for flares ($T_{\rm eff} \approx 9\,000 - 10\,000$ K) to estimate the incident UV flux. Given that a 9 000 K blackbody produces 84% less FUV emission than NUV emission, small temperature deviations from the adopted spectral energy distribution (SED) can produce large variations in the incident UV flux.

While large-scale observational studies of stellar flares have primarily been conducted in the optical wavelengths (e.g., Walkowicz et al. 2011; Shibayama et al. 2013; Hawley et al. 2014; Davenport 2016; Schmidt et al. 2019; Rodríguez Martínez et al. 2020; Günther et al. 2020; Feinstein et al. 2020), these wavelengths can comprise a small fraction of a flare's total emission (Maehara et al. 2012; Namekata et al. 2017). As displayed in Figure 1(a), the filter responses for the *Kepler* space telescope (Borucki et al. 2010), the Transiting Exoplanet Survey Satellite (*TESS,* Ricker et al. 2015) and the All-Sky Automated Survey for Supernovae (ASAS-SN, Shappee et al. 2014; Kochanek et al. 2017; Hart et al. 2023) capture only the Rayleigh-Jeans tail of blackbody emission for $T_{\rm eff} > 7\,000$ K. In addition, NUV and optical flare emission may arise from M-dwarf stars' chromospheres and upper photospheres (Joshi et al. 2021), whereas far-ultraviolet emission stems from the upper chromosphere and may correspond to the flare's impulsive phase of heating and compression of plasma (Neupert 1968; Dennis & Zarro 1993; Hawley et al. 2003; Benz & Güdel 2010).

While NUV and optical emission may be well-represented by a blackbody, some superflares have exhibited significant line emission in the FUV, sometimes surpassing quiescent flux levels by a factor of 100 (France et al. 2016). Loyd et al. (2018) computed a blackbody temperature of 15 500 K for the "Hazflare" in FUV spectra from the HST Cosmic Origins Spectrograph (COS, 1170−1430 Å). This flare exhibited substantial enhancements in C III, Si IV, S III, and N V emission lines; however, as with the 1985 Great Flare on AD Leo (Hawley & Pettersen 1991), a hot blackbody continuum dominated the total FUV emission. Furthermore, Froning et al. (2019) obtained a far/extreme-UV spectrum of the M dwarf GJ 674 with HST COS (1065 − 1365 Å) during a flare, revealing a blackbody-dominated spectrum with $T_{\rm eff} \approx 40\,000$ K and numerous superimposed C, Si, N, and Fe emission lines.

In contrast, FUV spectra of the Sun show flare emission dominated by line emission instead of a thermal continuum (Brekke et al. 1996; Simões et al. 2019). Given the intrinsic differences between M-dwarf and solar magnetic fields (and thus flare activity; Günther et al. 2020), it remains unclear when line emission dominates or continuum dominates for a given flare.

A more direct method for studying the impact of flares on habitability is time-resolved UV photometry of stars during flares. The NASA *Galaxy Evolution Explorer (GALEX)* space mission (Martin et al. 2005; Morrissey et al. 2007) provides a unique opportunity to study ultraviolet emission from flares. *GALEX* simultaneously observed in the far-ultraviolet (FUV: 1350 − 1750 Å) and near-ultraviolet (NUV: 1750 − 2750 Å) bands (Mar-

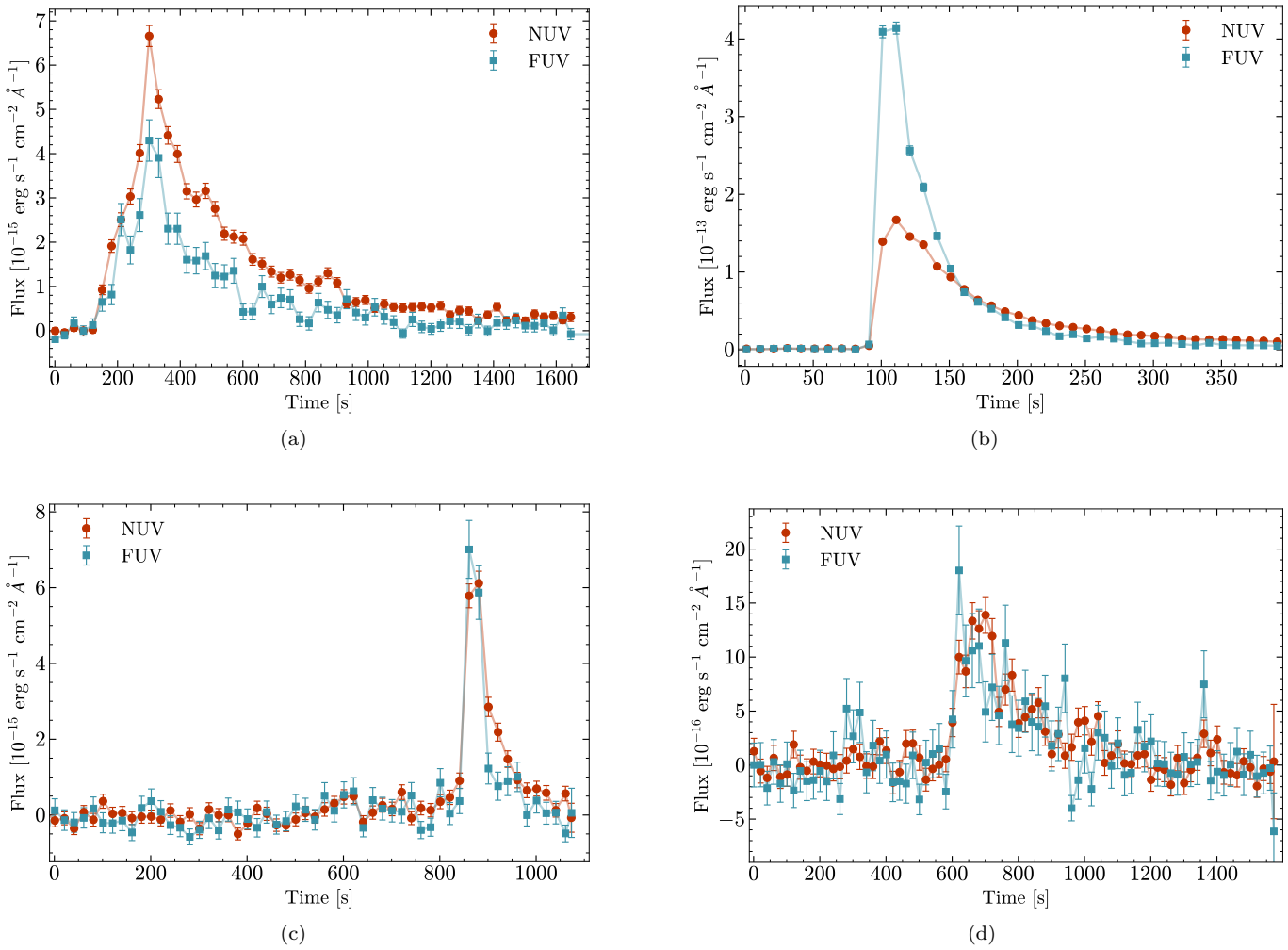

Figure 2. Example NUV and FUV light curves for two flares in our sample that are representative of the range of FUV/NUV flux and SNR we observe. *Upper panel:* Two high SNR flares spanning the range of FUV/NUV fluxes present in our sample. On the left is Gaia 3537511712697046656, a K6V star 56 pc from Earth. On the right is Gaia 1461125613285603840, an M4V star 13 pc from Earth. *Lower panel:* Flares chosen randomly from our sample. On the left is Gaia 3655483473505419 52, an M1.5V star 22 pc from Earth. On the right is Gaia 3858896247076028288, an M3.5V star 15 pc from Earth.

tin et al. 2005). In addition, the micro-channel plate detectors aboard *GALEX* recorded the timing of individual photon events to ≈ 5 ms precision. We can therefore construct high-cadence light curves with gPhoton (Million et al. 2016) to process *GALEX* observations at arbitrary time resolution.

Early flare studies utilizing the time-resolved UV photometry of *GALEX* have been limited to small sample sizes. Studies of a few flares using simultaneous *GALEX* FUV and NUV observations have characterized increases in FUV/NUV flux during superflares reaching a maximum ratio of 13 in the most extreme case, a factor of > 50 higher than would be predicted by a 9 000 K blackbody (Robinson et al. 2005; Welsh et al. 2006). FUV emission from host stars can photolyze CO_2 in planetary atmospheres, producing atomic oxygen which can then recombine to form O_2 (Tian et al. 2014). Therefore, high ratios of FUV/NUV radiation such as that observed by these studies may produce sufficient abiotic atmospheric oxygen to constitute a false biosignature (Tian et al. 2014; Harman et al. 2015). In addition, high FUV/NUV ratios suggest that that the typical SED assumptions for flare studies may be underestimating the true energy and ionizing flux of superflares.

In this work, we investigate all stars within 100 pc that were observed by *GALEX* simultaneously in the NUV and FUV. We use a sample of 182 flares on 158 stars and show that this FUV excess emission is not restricted to superflares but a general characteristic of flares on low-mass stars.

Gaia EDR3 ID	RA [deg]	Dec [deg]	Distance [pc]	M_G [mag]	RP [mag]	Spectral Type
1013481650428107648	132.6026	46.3209	81.95 ± 0.15	14.22	13.09	M3V
1027636694403121664	130.6758	51.4823	60.10 ± 0.07	13.92	12.73	M3V
1047687216648750976	159.5389	59.4848	93.44 ± 0.56	16.77	15.41	M5V
1058559634300870400	162.0490	64.7243	96.62 ± 0.21	15.21	13.96	M4V
1059924128230565888	161.0179	67.0126	47.40 ± 0.03	13.66	12.50	M3V
1070172916631499520	150.0283	68.1115	76.99 ± 0.14	15.44	14.22	M3.5V
1073027695493625856	157.6594	68.5490	88.37 ± 0.14	14.39	13.19	M3.5V
1076599905693041280	156.8567	71.0655	95.87 ± 0.26	15.39	14.17	M3.5V
1113525010848246784	96.6996	71.1834	90.77 ± 0.42	16.80	15.50	M4.5V
1119235182751380736	140.6038	70.1558	91.59 ± 1.32	18.56	17.11	M6V
...	...	...	...	...	...	...

Table 1. Star properties; full table available in the online version of the manuscript.

In Section 2 we provide an overview of our sample and flare detection method. Section 3 characterizes FUV and NUV flare emission in comparison to blackbody temperatures. Section 4 discusses the implications of our findings for characterizing the impact of stellar flares on the habitability of orbiting exoplanets.

2. SAMPLE SELECTION AND FLARE DETECTION

We select our targets from the Gaia Catalogue of Nearby Stars (GCNS), which is complete down to spectral type M8 within 100 pc (Gaia Collaboration et al. 2021). We exclude sources within one FWHM (≈ 5.6 arcsec) of another star in the GCNS to avoid contamination. We then use the gPhoton database and processing software (Million et al. 2016) to search for *GALEX* coverage of stars in the GCNS and perform aperture photometry. We exclude data with flags from gPhoton corresponding to aperture or annulus events in pixels that are contiguous to a masked hotspot or the detector edge. We bin photon events at cadences scaled by the physical distance of the corresponding sources. Shorter bins are employed for nearby sources. For white-light flares, amplitude and duration are correlated (Maehara et al. 2015), and so we expect shorter flares to be fainter and thus only be visible in more nearby stars. More distant objects are binned with longer cadences to enhance signal-to-noise ratios. We use 10, 20, and 30 s bins for stars within 15 pc, between 15 - 50 pc, and between $50 - 100$ pc respectively.

We find that bright sources exhibit significant systematics. We remove any light curves with median flux brighter than 15.4 mag NUV, a limit established by examining 2000 randomly chosen light curves by eye. Visual examination of stellar images and their background light curves suggests that contaminated sources either have a high cross-correlation between background and source flux over time, or a high standard deviation in background flux. We minimize this contamination by also removing light curves with background flux with a median above 40 counts or standard deviation above 6 counts.

We use light curves in the NUV for flare detection because the *GALEX* NUV detector has better throughput and efficiency (Bianchi et al. 2014). The flare detection approach relies on finding data points that are inconsistent with noise in the light curve and representative of true source variability (e.g., Chang et al. 2015). We estimate a baseline flux by iteratively sigma-clipping the light curve 2σ above the median flux. Given a time period $[t_a, t_b]$ of a light curve, we compute the mean flux $\bar{f}_{ab}$ and standard deviation σ_{ab}. For the ith flux measurement with calculated uncertainty σ_i within the time period, we evaluate:

$$\frac{f_i - \bar{f}_{ab}}{\sqrt{\sigma_i^2 + \sigma_{ab}^2}} \geq n, \quad (1)$$

where a flux satisfying Equation 1 corresponds to an $n\sigma$ detection. We first search for an individual 3σ detection in the light curve and then look to the neighboring points in the range $[t_{i-2}, t_{i+2}]$, excluding t_i. If there are two adjacent points in this range corresponding to 2σ detections we then flag the visit as containing a flare. Finally, we require that the flux does not peak at the first or last photometric point in the visit since some objects show decreasing or increasing trends only at the very beginning or end of a visit.

For this study we only include flares with observations in both FUV and NUV to enable the calculation of color temperatures. A full analysis of all light curves, including NUV-only flares and injection-recovery tests, is reserved for a forthcoming paper (Berger et al. in

Table 2. Flare properties; full table available in the online version of the manuscript.

Gaia EDR3 ID	t_{start}	t_{end}	Exp. Time	$\mathcal{R}_E$	$\mathcal{R}_{\lambda L\lambda}$	UV Energy
	[*GALEX* s]	[*GALEX* s]	[s]			[erg]
1013481650428107648	794114866	794115011	145	0.57 ± 0.06	1.16 ± 0.09	$1.96^{+0.10}_{-0.10}$e+32
1027636694403121664	823888055	823888475	420	0.39 ± 0.03	0.75 ± 0.04	$2.93^{+0.09}_{-0.09}$e+32
1047687216648750976	890596076	890596136	60	0.84 ± 0.21	1.16 ± 0.21	$4.70^{+0.60}_{-0.60}$e+31
1058559634300870400	758796977	758797577	600	0.78 ± 0.04	0.65 ± 0.05	$4.00^{+0.17}_{-0.17}$e+32
1059924128230565888	820629087	820629182	100	0.81 ± 0.23	1.20 ± 0.39	$9.03^{+1.44}_{-1.37}$e+30
1069666346712783488	882307565	882308342	777	0.50 ± 0.07	0.46 ± 0.14	$2.28e^{+0.16}_{-0.16}$+32
1070172916631499520	820545790	820545880	90	0.30 ± 0.16	0.52 ± 0.21	$2.09e^{+0.35}_{-0.35}$+31
1073027695493625856	882461389	882462136	748	0.48 ± 0.02	0.92 ± 0.03	$3.06e^{+0.04}_{-0.04}$+33
1076599905693041280	859394503	859394653	150	0.48 ± 0.08	0.59 ± 0.09	$1.31e^{+0.10}_{-0.10}$+32
1113525010848246784	912762216	912762336	120	0.74 ± 0.15	1.54 ± 0.23	$7.87^{+0.82}_{-0.84}$e+31
...	...	...	...	...	...	...

prep). As a final cut, we require that the FUV light curve has fewer than 3 missing observations within 5 points of peak NUV flare brightness. This method produces 188 candidates. Even with our quality cuts, six additional sources display variability that we classify as a false-positive upon examining the light curves and 2D images. These candidates appear within crowded fields.

Our final sample is composed of 182 flares with simultaneous observations in the NUV and FUV. We present their sources in Table 1. Spectral classification of our sample is discussed in Section 3.3 but the sample is composed of 79% fully convective stars ($\geq$ M3, $n = 143$), 16% partially convective M stars ($n = 30$), and 5% K stars ($n = 9$). Figure 2 displays the range of light curves we observe; the top panel shows two high signal-to-noise flares that span the range of FUV/NUV flux we observe, and the lower panel shows two representative randomly selected flares in our sample.

3. FUV FLARE EMISSION

In this section we calculate FUV/NUV emission ratios, inferred temperatures and UV energies for the 182 flares in our sample, summarized in Table 2, then compare the inferred blackbody color temperatures to the typically-assumed 9 000 K blackbody SED for flares.

3.1. *Flare temperatures assuming blackbody emission*

Under the assumption that the spectral energy distribution of a flare can be well-represented as a blackbody, we can construct a one-to-one relation between blackbody temperature and FUV/NUV λL_λ ratio. We do this by integrating the transmission function and blackbody SED over the range of wavelengths covered by each filter (Koornneef et al. 1986). We assume interstellar extinction is negligible since our sources are within the Local Bubble (e.g., Cox & Reynolds 1987; Fossati et al. 2017), characterized by a low-density interstellar medium. Figure 1(b) shows the FUV/NUV λL_λ ratio for a range of blackbody temperatures computed using synthetic photometry. Note that the color-temperature curve flattens considerably around 50 000 K, where both *GALEX* filters land on the Rayleigh-Jeans tail of the blackbody and thus the FUV-NUV color can no longer distinguish between hotter temperatures. The color-temperature curve asymptotes to FUV/NUV = 4.33 for arbitrarily high $T_{\rm eff}$.

We estimate the inferred blackbody temperature for each observation during a flare by directly measuring the FUV/NUV λL_λ ratio. Uncertainties on the color temperature are estimated by propagating the uncertainties on observed fluxes.

3.2. *Excess FUV emission*

We estimate the FUV excess flux for each observation during a flare by scaling a 9 000 K blackbody to the observed NUV flux. Then, we impute the expected FUV emission for comparison to our observations. We denote the ratio of time-integrated energies by $\mathcal{R}_E = E_{\rm FUV}/E_{\rm NUV}$.

A 9 000 K blackbody produces a time-integrated energy ratio of 0.17 whereas we find a median $\mathcal{R}_E = 0.50$ ($T_{\rm eff} \approx 13\,500$ K) and a maximum $\mathcal{R}_E = 1.06$ ($T_{\rm eff} \approx 21\,000$ K). Thus, a 9 000 K blackbody underestimates the median observed $\mathcal{R}_E$ by a factor of 3.0 and underestimates the maximum ratio by a factor of 6.3. Among the flares in our sample, 98% ($n = 178$) display $\mathcal{R}_E$ ratios that exceed expectations for a 9 000 K blackbody. This suggests that a constant 9 000 K black-

body SED is insufficient to account for the levels of FUV emission we observe.

On the other hand, FUV/NUV ratios at individual epochs in a flare can significantly exceed the time-integrated values. To quantify this, we compute the observed ratios of FUV/NUV λL_λ at peak NUV brightness for each flare, which we refer to as $\mathcal{R}_{\lambda L\lambda}$. Figures 3(b) and 4(b) show the $\mathcal{R}_{\lambda L\lambda}$ values with respect to spectral type and flare UV energy. Note that relying on the NUV time of peak introduces a slight bias against NUV-faint flares. Thus, true FUV/NUV ratios are likely higher around flare peak. This behavior is demonstrated in Figure 2(c), where the observed FUV flux both exceeds the NUV flux and peaks before the NUV.

We find a median $\mathcal{R}_{\lambda L\lambda}= 0.57$ ($T_{\rm eff} \approx 14\,300$ K) and a maximum $\mathcal{R}_{\lambda L\lambda}= 2.12$ ($T_{\rm eff} \approx 49\,600$ K). Thus, a 9 000 K blackbody underestimates the median observed $\mathcal{R}_{\lambda L\lambda}$ by a factor of 3.4 and underestimates the maximum ratio by a factor of 12.6.

3.3. *Results by spectral type*

Stellar magnetic fields, which are the energy sources for stellar flares, originate from dynamo-related convective motions and differential rotation, (e.g., Pettersen 1989; Balona et al. 2015; Doorsselaere et al. 2017) and so the depth of the convection zone may correlate with flare properties. To test this idea, we derive spectral types for the flare stars in our sample using Gaia G-RP color (Gaia Collaboration et al. 2021) and the spectral type-color sequence from Pecaut & Mamajek (2013), estimating a fully convective boundary of M3V (Jao et al. 2018). We use this system because we do not have rotation periods for every star in the sample to compute a Rossby number. We divide our sample into three spectral classification bins: K stars, partially convective M dwarfs (M0V-M2V), and fully convective stars (M3+). Figures 3(a) and 3(b) illustrate the distributions of time-integrated energy ratios $\mathcal{R}_E$ and $\mathcal{R}_{\lambda L\lambda}$ by spectral bin. Table 3 displays the medians and standard deviations for each kernel density estimate (KDE).

There appears to be a trend with an increasing median $\mathcal{R}_{\lambda L\lambda}$ with later spectral types and thus deepening convective envelopes. The distribution of $\mathcal{R}_{\lambda L\lambda}$ for K stars has a median of 0.443 (12 700 K); M0V-M2V stars a median $\mathcal{R}_{\lambda L\lambda}$ of 0.541 (14 000 K); and fully convective stars a median $\mathcal{R}_{\lambda L\lambda}$ of 0.577 (14 400 K). The $\mathcal{R}_E$ distributions peak at similar values but skew towards higher ratios, a similar trend to $\mathcal{R}_{\lambda L\lambda}$. Furthermore, fully convective stars exhibit the largest deviations from the assumed 9 000 K blackbody.

We explore the significance of these findings in three ways:

1) As a first attempt, we pairwise compared the spectral type categories using Kolmogorov-Smirnov (K-S) and Anderson-Darling tests. Neither of these tests were able to differentiate either the $\mathcal{R}_E$ or $\mathcal{R}_{\lambda L\lambda}$ distributions at 95% confidence.

2) As a next attempt, we bootstrapped the mean ratios for each spectral type category. We resampled each category with replacement 10 000 times and calculated the mean of the distribution. We compute $\mathcal{R}_E$ means and quantile intervals for K, early M, and fully convective stars of 0.49 ± 0.05, 0.49 ± 0.03, and 0.52 ± 0.02. We compute $\mathcal{R}_{\lambda L\lambda}$ means and quantile intervals for K, early M, and fully convective stars of 0.45 ± 0.08, 0.53 ± 0.04, and $0.59^{+0.02}_{-0.03}$, respectively. The appears to be a statistically significant correlation between $\mathcal{R}_{\lambda L\lambda}$ and spectral type.

3) Finally, we explore a potential linear relationship between the FUV/NUV ratios and *G-RP* color as a proxy for spectral type (shown in Figure 3(e) and 3(f)). As a first step, we cut obvious outliers, five with negative $\mathcal{R}_{\lambda L\lambda}$ and two with large but very uncertain $\mathcal{R}_{\lambda L\lambda}$. The Pearson correlation coefficient is 0.18 for $\mathcal{R}_{\lambda L\lambda}$ vs. *G-RP* and 0.06 for $\mathcal{R}_E$ vs. *G-RP*. These indicate a tentative weak correlation but the significance is difficult to determine because the Pearson correlation coefficient does not consider uncertainties. Instead, we will perform a linear fit and bootstrap the sample to determine if there is a statistically significant positive slope. First, to reduce the covariance between the slope and intercept we move the intercept to the median color of the sample as given by:

$$\mathcal{R} = m \times (\log_{10}(\mathrm{E_{UV}}/\mathrm{erg}) - 1.2) + b, \qquad (2)$$

for slope m, intercept b, and ratio $\mathcal{R}$ (either $\mathcal{R}_E$ or $\mathcal{R}_{\lambda L\lambda}$). Second, to account both for underestimated errors and for the intrinsic scatter in the flare population, we iteratively fit a best-fit line adding increasing uncertainty in quadrature with the $\mathcal{R}_E$ or $\mathcal{R}_{\lambda L\lambda}$ uncertainties until a reduced $\chi^2 = 1$ was found for each fit. We report the best-fit values in Table 4 and show the best-fits in Figures 3(e) and 3(f). Next we determine the uncertainty on the linear fit by bootstrapping the sample with replacement 10 000 times. We show 100 randomly selected bootstrapped fits in Figures 3(e) and 3(f) to indicate the fit uncertainty. In Table 4 we report the 16^{th} and 84^{th} percentile along with the percentage of the resamples where the slope of the best fit is ≤ 0. Finally, to verify the least-square fits are not being driven by outliers, we redo the linear fits using Theil-Sen Regression, bootstrap the fits, and also report those fits in Table 4. We then take the fraction of bootstrap trials with slopes ≤ 0 as our p-value for the detection of a positive relation.

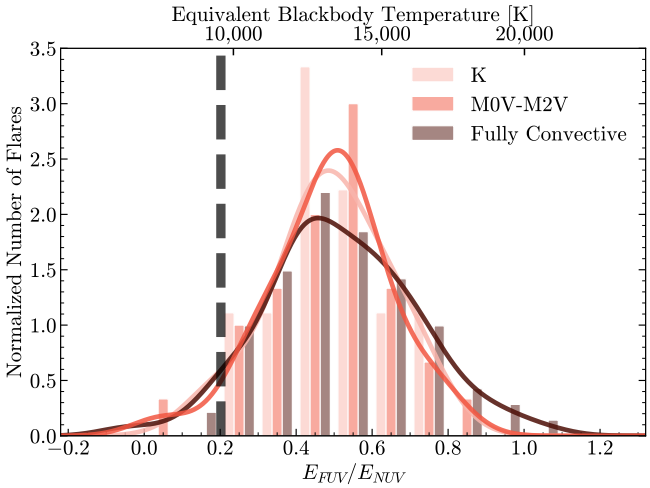

(a) Energy ratio

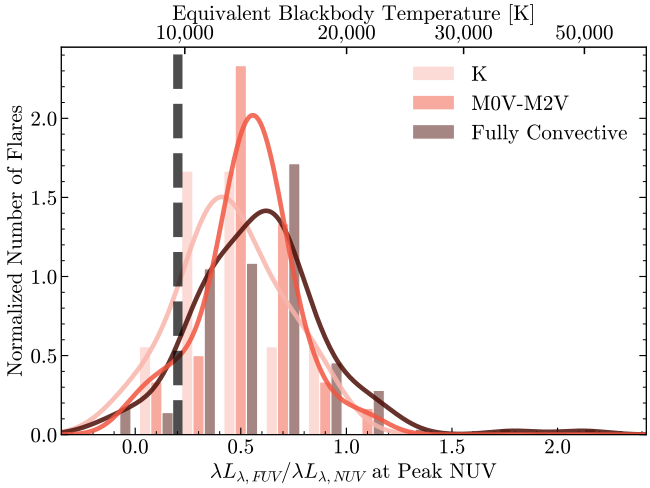

(b) λL_λ ratio at peak NUV

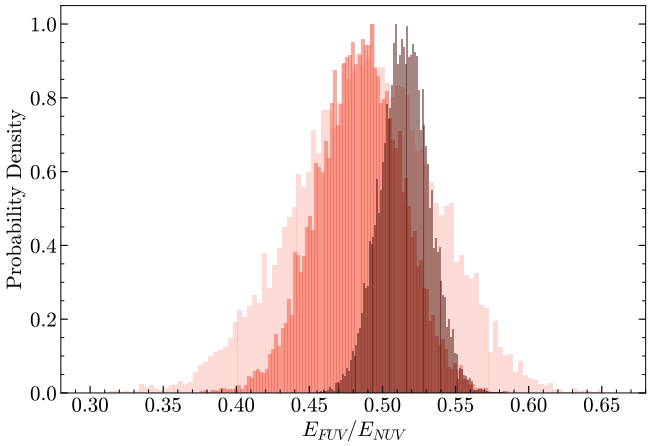

(c) Bootstrapped energy ratio

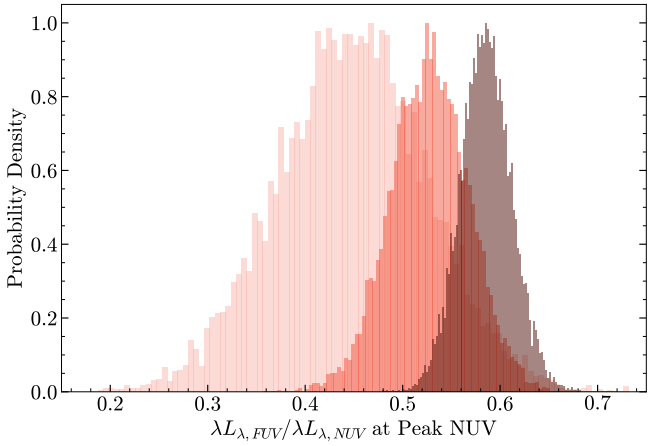

(d) Bootstrapped λL_λ ratio

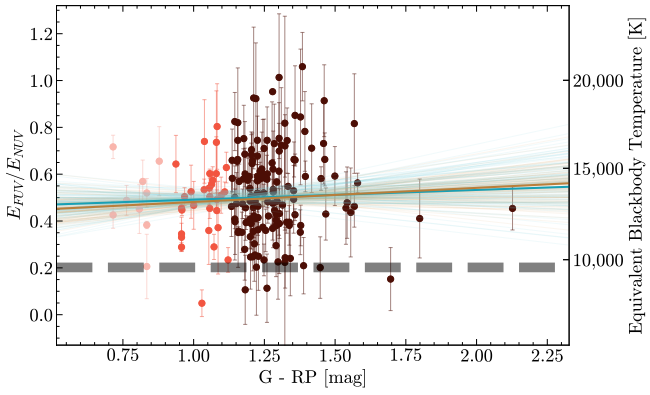

(e) Energy ratio vs. G-RP color

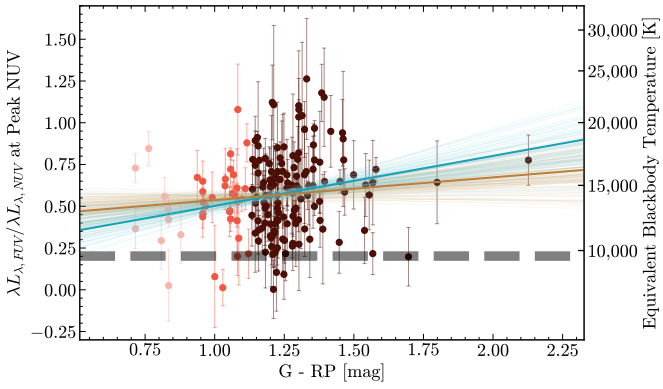

(f) λL_λ ratio vs. G-RP color

Figure 3. Histograms and scaled kernel density estimates (top), bootstrapped mean values (middle), and scatter plots with lines of best fit (bottom) for FUV/NUV energy ratios (left) and λL_λ at peak NUV flux (right), with respect to spectral type. The ratios corresponding to $9\,000 - 10\,000$ K blackbody SEDs are denoted by vertical and horizontal black dashed lines in the top and bottom panels, respectively. Blackbody temperatures corresponding to their respective FUV/NUV ratios are marked on the top axis. X-axes are not consistent between panels. Lines of best fit on the bottom panel are computed using least-squares optimization (orange) and Theil-Sen regression (turquoise). Color darkens with spectral type; ratios for K stars are plotted in light pink, partially convective M stars in red, and fully convective stars in brown.

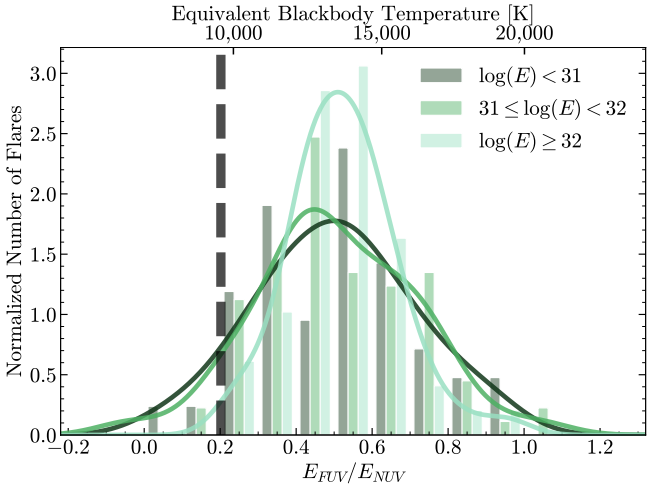

(a) Energy ratio

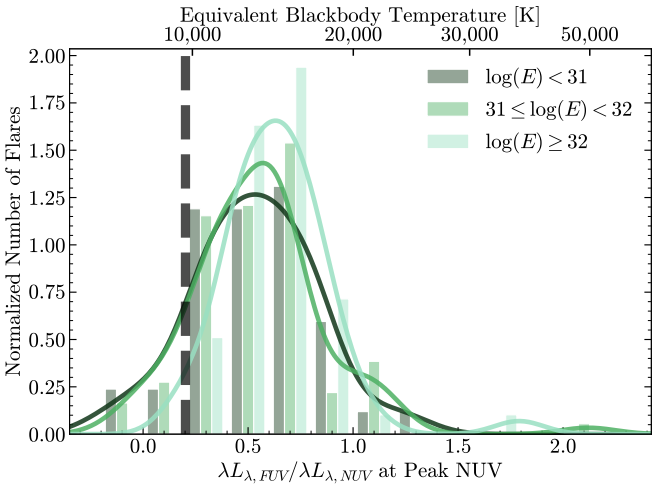

(b) λL_λ ratio at peak NUV

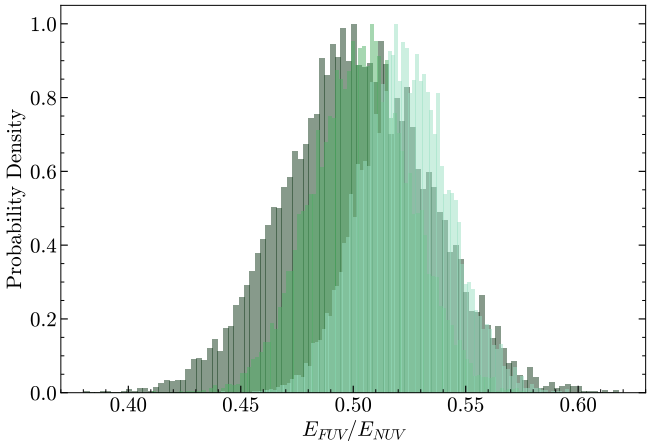

(c) Bootstrapped energy ratio

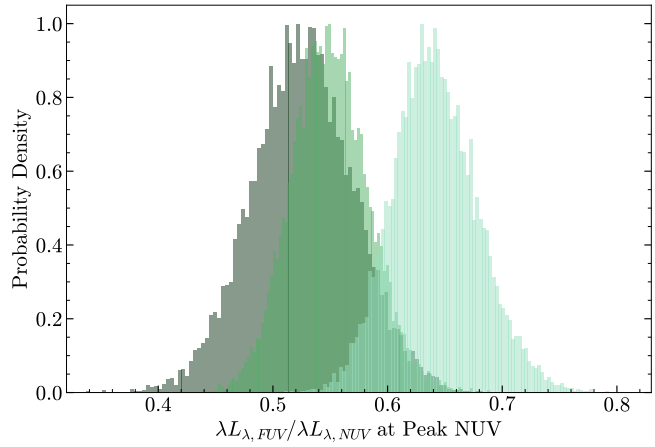

(d) Bootstrapped λL_λ ratio

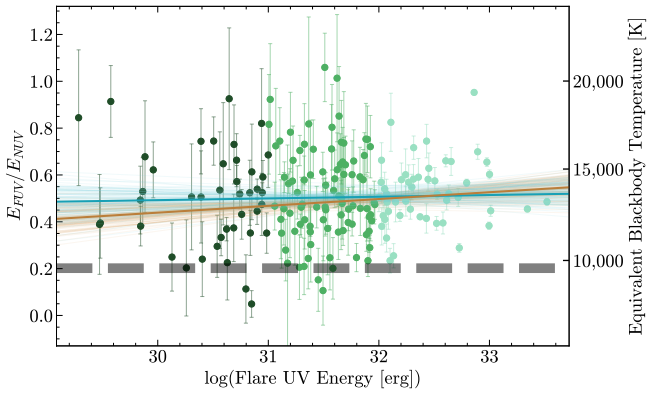

(e) Energy ratio vs. log(flare energy)

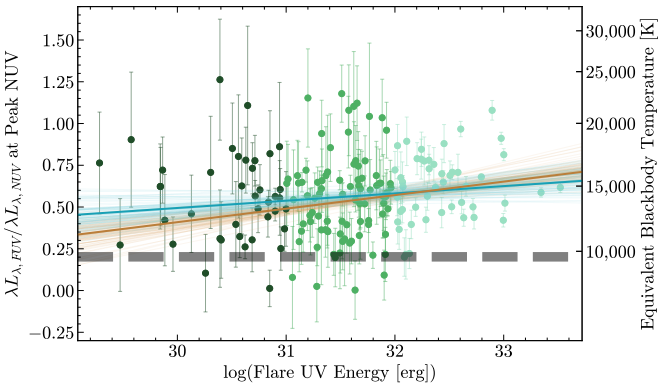

(f) Energy ratio vs. log(flare energy)

Figure 4. Same as Figure 3, but with respect to UV flare energy. Color lightens with an increase in UV flare energy; ratios corresponding to energies below 10^{31} erg in dark green, to UV energies between $10^{31} - 10^{32}$ erg in medium green, and to energies of 10^{32} erg or higher in light green.

When reporting the significance, we take the more conservative value between the least-square and Theil-Sen fits. We find that the $\mathcal{R}_{\lambda L\lambda}$ vs. color slope is consistent with being positively correlated at nearly 2 sigma and the $\mathcal{R}_E$ vs. color slope is consistent with being positively correlated at nearly 1.5 sigma.

Thus we conclude there is a tentative trend with increasing average $\mathcal{R}_{\lambda L\lambda}$ and $\mathcal{R}_E$ with later spectral types, especially for $\mathcal{R}_{\lambda L\lambda}$ and for fully convective stars. However, we note that the uncertainties of the $\mathcal{R}_{\lambda L\lambda}$ and $\mathcal{R}_E$ ratios are large relative to the difference in the means between spectral type categories.

3.4. *Results by flare UV energy*

We also investigate for trends between the total flare UV energy and FUV/NUV ratio. First, we estimate the total UV flux at each epoch by fitting a linear SED between $(\lambda_{\rm eff}^{\rm FUV}, f_{\rm FUV})$ and $(\lambda_{\rm eff}^{\rm NUV}, f_{\rm NUV})$ for an observed FUV flux $f_{\rm FUV}$ and corresponding NUV flux $f_{\rm NUV}$ and effective wavelengths $\lambda_{\rm eff}^{\rm FUV} = 1528$ Å and $\lambda_{\rm eff}^{\rm NUV} = 2271$ Å (Morrissey et al. 2005). We integrate the linear SED over the wavelength range covered by 10% of peak filter response for the *GALEX* filters, 1343- − 2831 Å, as shown in Figure 1(a). We then use the distance from Gaia as presented in Table 1 to compute total flare UV energies ($E_{\rm UV}$). We find that our flare sample has $E_{\rm UV} = 2 \times 10^{29} - 3 \times 10^{33}$ erg, with a median UV energy of 3.8×10^{31} erg.

We divide the flare sample into 3 bins of $E_{\rm UV}$, flares with $E_{\rm UV} < 10^{31}$ erg, $10^{31} < E_{\rm UV} < 10^{32}$ erg, and $E_{\rm UV} > 10^{32}$ erg. Figures 4(a) and 4(b) display $\mathcal{R}_E$ and $\mathcal{R}_{\lambda L\lambda}$ as a function of $E_{\rm UV}$. The corresponding values of the kernel density estimates by UV energy are noted in Table 3. The distribution of $\mathcal{R}_{\lambda L\lambda}$ for flare UV energies below 10^{31} erg has a median of 0.530 (13 800 K); energies between $10^{31}-10^{32}$ erg a median of 0.535 (13 900 K); and energies 10^{32} erg and above a median of 0.628 (15 000 K).

We then perform similar statistical tests as in Section 3.3.

1) K-S and Anderson Darling tests again can mostly not distinguish the $\mathcal{R}_E$ or $\mathcal{R}_{\lambda L\lambda}$ distributions for the $E_{\rm UV}$ groups. However, the K-S test between the $10^{31} < E_{\rm UV} < 10^{32}$ erg and $E_{\rm UV} > 10^{32}$ erg $\mathcal{R}_{\lambda L\lambda}$ samples has a marginal, p-value of 0.03, detection that they are drawn from different distributions.

2) We compute $\mathcal{R}_E$ means and quantile intervals for flare energies of $E_{\rm UV} < 10^{31}$ erg, $10^{31} < E_{\rm UV} < 10^{32}$ erg, and $E_{\rm UV} > 10^{32}$ erg of 0.50±0.03, 0.51±0.02, and 0.52±0.02. We compute $\mathcal{R}_{\lambda L\lambda}$ means and quantile intervals of 0.53± 0.04, 0.55 ± 0.03, and 0.64 ± 0.04, respectively. There appears to be a statistically significant trend where the most energetic flares have a higher $\mathcal{R}_{\lambda L\lambda}$ but it does not appear such a relation exists for $\mathcal{R}_E$.

3) We follow the same procedure as in Section 3.3 investigating if there is a linear relationship between FUV/NUV ratios and $E_{\rm UV}$. First, the Pearson correlation coefficient is 0.11 for $\mathcal{R}_{\lambda L\lambda}$ vs. $E_{\rm UV}$ and 0.02 for $\mathcal{R}_E$ vs. $E_{\rm UV}$. These indicate a tentative weak correlation but we bootstrap least-squares and Theil-Sen linear fits to test their statistical significance. Again to reduce covariance between the fit parameters we choose a pivot near the median $E_{\rm UV}$ as shown by:

$$\mathcal{R} = m \times (\log_{10}(\mathrm{E_{UV}/erg}) - 31.6) + b, \qquad (3)$$

for slope m, intercept b, and ratio $\mathcal{R}$. The best-fits are shown in Figures 4(e) and 4(f). In Table 4 we report the fit statistics. We find that the $\mathcal{R}_{\lambda L\lambda}$ vs. $E_{\rm UV}$ slope is consistent with being positively correlated at $\gtrsim 2$ sigma. However, the outlier-resistant Theil-Sen fit is consistent with no relationship between $\mathcal{R}_E$ and $E_{\rm UV}$.

Thus we conclude there is a trend with increasing $\mathcal{R}_{\lambda L\lambda}$ for more UV luminous flares, especially for the largest ($E_{\rm UV} > 10^{32}$ erg) flares. However, we do not find evidence for a similar trend with $\mathcal{R}_E$.

4. POTENTIAL IMPACTS ON HABITABILITY

We have demonstrated that uniformly selected field stars exhibit flares that are FUV luminous and not well-represented by a constant 9 000 − 10 000 K blackbody. This finding holds for observed fluxes, integrated energy and peak luminosity. In this section, we discuss some implications of this finding.

Ultraviolet-C radiation (UVC, ∼2000-2800 Å) is expected to drive prebiotic chemistry (Todd et al. 2018; Rimmer et al. 2018) and ozone depletion (Segura et al. 2010; Tilley et al. 2019). If blackbody temperatures during flares indeed exceed 9 000 K, then flares deliver higher levels of NUV flare radiation than assumed when characterizing the impact of flaring on abiogenesis and atmospheric ozone depletion.

Optical studies of flares and their potential impact on exoplanet habitability typically assume a constant 9 000 K blackbody for flares, which impacts their calculation of flare energy (Schmidt et al. 2019; Rodríguez et al. 2018; Günther et al. 2020; Zeldes et al. 2021; Bogner et al. 2021). Zeldes et al. (2021) selected a sample of five superflaring stars and found that none fell into either zone.

In a sample of 1228 flaring stars from TESS, Günther et al. (2020) found eight percent of sources to display sufficient flaring rates and energies to fall into the ozone depletion zone, and only one percent to fall in the abiogenesis zone. If instead these flares are well-represented

Table 3. Kernel Density Estimates

	$\mathcal{R}_E$ median	16th percentile	84th percentile	$\mathcal{R}_{\lambda L \lambda}$ median	16th percentile	84th percentile
$\log(E_{UV} < 31)$	0.501	0.277	0.734	0.530	0.219	0.833
$31 \leq \log(E_{UV}) < 32$	0.497	0.289	0.739	0.535	0.242	0.829
$\log(E_{UV}) \geq 32$	0.518	0.382	0.662	0.628	0.395	0.865
K	0.494	0.320	0.666	0.443	0.178	0.739
Early M	0.493	0.318	0.652	0.541	0.301	0.743
Fully Convective	0.509	0.313	0.725	0.577	0.284	0.863

Table 4. Fits to FUV/NUV trends with respect to G-RP color and flare UV energy.

	Best-fit slope Best-fit m	Best-fit intercept Best-fit b	16th percentile slope 16th percentile m	84th percentile slope 84th percentile m	16th percentile intercept 16th percentile b	84th percentile intercept 84th percentile b	% slope ≤ 0 % $m \leq 0$
Least-squares fit							
$\mathcal{R}_{\lambda L \lambda}$ vs. G-RP	0.14	0.56	0.05	0.23	0.55	0.58	6.80
$\mathcal{R}_{\lambda L \lambda}$ vs. UV energy	0.08	0.54	0.05	0.10	0.52	0.56	0.04
$\mathcal{R}_E$ vs. G-RP	0.06	0.49	0.00	0.13	0.48	0.51	16.25
$\mathcal{R}_E$ vs. UV energy	0.03	0.49	0.01	0.05	0.47	0.50	4.65
Theil-Sen fit							
$\mathcal{R}_{\lambda L \lambda}$ vs. G-RP	0.24	0.56	0.13	0.30	0.55	0.58	0.30
$\mathcal{R}_{\lambda L \lambda}$ vs. UV energy	0.04	0.56	0.02	0.07	0.54	0.58	3.80
$\mathcal{R}_E$ vs. G-RP	0.09	0.50	0.00	0.16	0.49	0.52	18.95
$\mathcal{R}_E$ vs. UV energy	0.00	0.50	0.00	0.03	0.48	0.52	31.15

by 13 500 K blackbody SED, the number of stars with sufficient flaring activity to fall in the ozone depletion zone would increase by 60%. In particular, the number of early M stars (M0-M4) in the ozone depletion zone would increase by 270%.

Characterizing the impact of higher flare temperatures on prebiotic chemistry is less straightforward. Rimmer et al. (2018) assumes an Earth-like atmosphere which will absorb wavelengths shorter than 2100 Å, and focuses on NUV radiation (2000 − 2800 Å) as a driver of prebiotic chemistry. Rimmer et al. (2018) estimates the total number of photons between 2000 − 2800 Å reaching a planet's surface by assuming the AD Leo flare spectrum in their model is flat at wavelengths shorter than the U band. We found this is likely not the case in the FUV (1350 − 1750 Å) and NUV (1750 − 2750 Å). This calls into question their conclusion that the number of NUV photons reaching a planet's surface can be inferred from the U-band flare energy.

In future work (Berger et al. 2024, in prep) we will directly compute population-averaged NUV flare rate distributions, directly probing the wavelength ranges thought to be important for the formation of complex molecules. Naively scaling a blackbody in TESS from 9000 K to 13 500 K will result in an increase in NUV photons by a factor 3.86.

UV radiation from stars impacts the atmospheric composition of orbiting planets. Large ratios of FUV/NUV radiation as seen on M dwarfs may produce sufficient abiotic atmospheric oxygen to produce a false biosignature (Tian et al. 2014; Harman et al. 2015). These studies characterize UV radiation in steady state and do not account for flaring events. Additional modeling work should be undertaken to investigate if the stronger FUV flux during flares that we observe in this work can significantly alter atmospheric oxygen abundances and thus affecting interpretation of exo-atmospheric signatures. A few FUV spectra of flares exist (Hawley & Pettersen 1991; France et al. 2016; Loyd et al. 2018; Froning et al. 2019) but the short timescales of flares make obtaining these observations difficult.

We identified no observations with FUV/NUV flux ratios above the 4.33 $\mathcal{R}_E$ asymptote in our color-temperature curve (Figure 1(b)) above which the overall FUV emission could not be attributed solely to blackbody emission. Thus for the stars in our sample, we cannot determine the extent to which line emission contributes to the total FUV emission we observe. To characterize the respective contributions of line and continuum emission to overall FUV flare emission will require obtaining FUV spectra of a population of stars in quiescence and flare. Spectral observations of a large solar flare suggest that line emission can indeed dominate the overall UV flare emission (Simões et al. 2019). Our results highlight the importance of simultaneous observations of flares across the electromagnetic spectrum in order to fully capture the emission processes involved (e.g., Paudel et al. 2021).

Looking forward, two missions planned for launch in 2026 may advance our understanding of stellar flares in the ultraviolet. The Ultraviolet Transient Astronomy Satellite (ULTRASAT; Shvartzvald et al. 2023) plans to observe $> 10^5$ flaring and variable stars in the NUV (2300 − 2900 Å), sensitive to < 23.5 AB mag. ULTRASAT will provide insight into the levels of NUV radiation from flares that may drive prebiotic chemistry or atmospheric ozone depletion. However, the single-filter design of ULTRASAT will not allow any temperature estimates. Additionally, the Monitoring Activity of Nearby sTars with uv Imaging and Spectroscopy (MANTIS; Indahl & Wilson 2022) mission will work alongside JWST and may be a better probe of flare energetics. MANTIS will observe cool stars in the extreme-ultraviolet (100 − 900 Å), far-ultraviolet (900 − 2000 Å), near-ultraviolet (2000 − 3200 Å), and visible (3200 − 10 000 Å) wavelengths, providing a detailed estimate of the color temperature. MANTIS will provide the first glimpse at many stars in the EUV, and may shed light on the proportion of flare radiation originating from continuum versus UV line emission.

5. CONCLUSIONS

In this work, we have identified 182 flares on 158 stars with simultaneous observations in the NUV and FUV from the *GALEX* space telescope. We select our targets from the Gaia Catalogue of Nearby Stars which is complete down to spectral type M8 within our survey volume of 100 pc. Thus, this study suffers from minimal selection basis. We have computed color temperatures at each epoch of the flares in our sample using a derived relation between FUV/NUV flux and blackbody temperature. Our main results are as follows.

1. A constant 9 000 K blackbody underpredicts the FUV emission for 98% of flares in our sample.

2. The FUV/NUV ratio at peak appears to positively correlate ($\sim 2\sigma$ significance) both with total UV flare energy and with increasing $G - RP$ color of the host star.

Future work (Berger in prep.) will use this *GALEX* flare sample and an injection and recovery analysis to compute the UV flare rate distribution and produce a UV flare model.

ACKNOWLEDGEMENTS

VLB acknowledges support from the Research Experience for Undergraduates program at the Institute for Astronomy, University of Hawaii-Manoa funded through NSF grant #2050710. VLB thanks the Institute of Astronomy for its hospitality over the course of this project. VLB is also supported by a Churchill Scholarship. JTH was supported by NASA grant 80NSSC21K0136. BJS is supported by NSF grants AST-1907570, AST-1920392 and AST-1911074. JvS acknowledges support from NASA grant 80NSSC22K0293. D.H. acknowledges support from the Alfred P. Sloan Foundation and the Australian Research Council (FT200100871). We thank Dr. Michael Liu and Dr. Allison Youngblood for useful discussions.

Software: `matplotlib` (Hunter 2007), `numpy` (Harris et al. 2020), `pandas` (Wes McKinney 2010), `scipy` (Virtanen et al. 2020), `astropy` (Astropy Collaboration et al. 2013, 2018, 2022).

DATA AVAILABILITY

This manuscript only uses publicly available data from *GALEX* and *Gaia*. All derived data products will be made publicly available upon publication.

REFERENCES

Astropy Collaboration et al., 2013, A&A, 558, A33

Astropy Collaboration et al., 2018, AJ, 156, 123

Astropy Collaboration et al., 2022, apj, 935, 167

Balona L. A., Broomhall A. M., Kosovichev A., Nakariakov V. M., Pugh C. E., Van Doorsselaere T., 2015, MNRAS, 450, 956

Benz A. O., Güdel M., 2010, ARA&A, 48, 241

Bianchi L., Conti A., Shiao B., 2014, Advances in Space Research, 53, 900

Bogner M., Stelzer B., Raetz S., 2021, Astronomische Nachrichten, 343

Borucki W. J., et al., 2010, Science, 327, 977

Brekke P., Rottman G. J., Fontenla J., Judge P. G., 1996, ApJ, 468, 418

Chang S. W., Byun Y. I., Hartman J. D., 2015, ApJ, 814, 35

Cox D. P., Reynolds R. J., 1987, ARA&A, 25, 303

Davenport J. R. A., 2016, ApJ, 829, 23

Dennis B. R., Zarro D. M., 1993, SoPh, 146, 177

Doorsselaere T. V., Shariati H., Debosscher J., 2017, The Astrophysical Journal Supplement Series, 232, 26

Endl M., Cochran W. D., Tull R. G., MacQueen P. J., 2003, The Astronomical Journal, 126, 3099

Feinstein A. D., Montet B. T., Ansdell M., Nord B., Bean J. L., Günther M. N., Gully-Santiago M. A., Schlieder J. E., 2020, AJ, 160, 219

Fossati L., et al., 2017, A&A, 601, A104

France K., et al., 2016, ApJ, 820, 89

Froning C. S., et al., 2019, A Hot Ultraviolet Flare on the M Dwarf Star GJ 674, doi:10.48550/ARXIV.1901.08647, https://arxiv.org/abs/1901.08647

Gaia Collaboration et al., 2021, A&A, 649, A6

Günther M. N., et al., 2020, The Astronomical Journal, 159, 60

Harman C. E., Schwieterman E. W., Schottelkotte J. C., Kasting J. F., 2015, ApJ, 812, 137

Harris C. R., et al., 2020, Nature, 585, 357

Hart K., et al., 2023, arXiv e-prints, p. arXiv:2304.03791

Hawley S. L., Pettersen B. R., 1991, ApJ, 378, 725

Hawley S. L., et al., 2003, ApJ, 597, 535

Hawley S. L., Davenport J. R. A., Kowalski A. F., Wisniewski J. P., Hebb L., Deitrick R., Hilton E. J., 2014, The Astrophysical Journal, 797, 121

Hunter J. D., 2007, Computing in Science & Engineering, 9, 90

Indahl B., Wilson D., 2022, MANTIS: Monitoring Activity from Nearby sTars with uv Imaging and Spectroscopy, NASA Prop. ID 22-APRA22-121

Jao W.-C., Henry T. J., Gies D. R., Hambly N. C., 2018, ApJL, 861, L11

Joshi R., Schmieder B., Heinzel P., Tomin J., Chandra R., Vilmer N., 2021, A&A, 654, A31

Kaltenegger L., Traub W. A., 2009, ApJ, 698, 519

Kochanek C. S., et al., 2017, PASP, 129, 104502

Koornneef J., Bohlin R., Buser R., Horne K., Turnshek D., 1986, Highlights of Astronomy, 7, 833

Litvinenko Y. E., 1999, ApJ, 515, 435

Loyd R. O. P., Shkolnik E. L., Schneider A. C., Barman T. S., Meadows V. S., Pagano I., Peacock S., 2018, The Astrophysical Journal, 867, 70

Maehara H., et al., 2012, Nature, 485, 478

Maehara H., Shibayama T., Notsu Y., Notsu S., Honda S., Nogami D., Shibata K., 2015, Earth, Planets and Space, 67, 59

Martin D. C., et al., 2005, ApJL, 619, L1

Million C., et al., 2016, ApJ, 833, 292

Morrissey P., et al., 2005, ApJL, 619, L7

Morrissey P., et al., 2007, ApJS, 173, 682

Namekata K., et al., 2017, ApJ, 851, 91

Neupert W. M., 1968, ApJL, 153, L59

Paudel R. R., et al., 2021, ApJ, 922, 31

Pecaut M. J., Mamajek E. E., 2013, ApJS, 208, 9

Pettersen B. R., 1989, SoPh, 121, 299

Reiners A., 2012, Living Reviews in Solar Physics, 9

Ricker G. R., et al., 2015, Journal of Astronomical Telescopes, Instruments, and Systems, 1, 014003

Rimmer P. B., Xu J., Thompson S. J., Gillen E., Sutherland J. D., Queloz D., 2018, Science Advances, 4

Robinson R. D., et al., 2005, ApJ, 633, 447

Rodríguez Martínez R., Lopez L. A., Shappee B. J., Schmidt S. J., Jayasinghe T., Kochanek C. S., Auchettl K., Holoien T. W. S., 2020, ApJ, 892, 144

Rodríguez R., et al., 2018, Research Notes of the American Astronomical Society, 2, 8

Schmidt S. J., et al., 2014, ApJL, 781, L24

Schmidt S. J., et al., 2016, ApJL, 828, L22

Schmidt S. J., et al., 2019, ApJ, 876, 115

Segura A., Walkowicz L. M., Meadows V., Kasting J., Hawley S., 2010, Astrobiology, 10, 751

Shappee B. J., et al., 2014, ApJ, 788, 48

Shibata K., Takasao S., 2016, in , Magnetic Reconnection. Springer International Publishing, pp 373–407, doi:10.1007/978-3-319-26432-5˙10, https://doi.org/10.1007%2F978-3-319-26432-5_10

Shibayama T., et al., 2013, ApJS, 209, 5

Shvartzvald Y., et al., 2023, arXiv e-prints, p. arXiv:2304.14482

Simões P. J. A., Reid H. A. S., Milligan R. O., Fletcher L., 2019, ApJ, 870, 114

Tian F., France K., Linsky J. L., Mauas P. J. D., Vieytes M. C., 2014, Earth and Planetary Science Letters, 385, 22

Tilley M. A., Segura A., Meadows V., Hawley S., Davenport J., 2019, Astrobiology, 19, 64

Todd Z. R., Fahrenbach A. C., Magnani C. J., Ranjan S., Björkbom A., Szostak J. W., Sasselov D. D., 2018, Chemical Communications, 54, 1121

Virtanen P., et al., 2020, Nature Methods, 17, 261

Walkowicz L. M., et al., 2011, AJ, 141, 50

Welsh B. Y., et al., 2006, A&A, 458, 921

Wes McKinney 2010, in Stéfan van der Walt Jarrod Millman eds, Proceedings of the 9th Python in Science Conference. pp 56 – 61, doi:10.25080/Majora-92bf1922-00a

Zeldes J., et al., 2021, arXiv e-prints, p. arXiv:2109.04501